

# Synchrotron scanning photoemission microscopy of homogeneous and heterogeneous metal sulfide minerals

Robert George Acres,<sup>a</sup> Sarah Louise Harmer,<sup>a</sup> Hung Wei Shui,<sup>b</sup> Chia-Hao Chen<sup>b</sup> and David Allan Beattie<sup>a\*</sup>

<sup>a</sup>Ian Wark Research Institute, University of South Australia, Mawson Lakes, South Australia 5095, Australia, and <sup>b</sup>National Synchrotron Radiation Research Centre, 101 Hsin-Ann Road, Hsinchu 300, Taiwan. E-mail: david.beattie@unisa.edu.au

Scanning photoemission microscopy (SPEM) has been applied to the investigation of homogeneous and heterogeneous metal sulfide mineral surfaces. Three mineral samples were investigated: homogeneous chalcopyrite, heterogeneous chalcopyrite with bornite, and heterogeneous chalcopyrite with pyrite. Sulfur, copper and iron SPEM images, *i.e.* surface-selective elemental maps with high spatial resolution acquired using the signal from the S 2*p* and Cu and Fe 3*p* photoemission peaks, were obtained for the surfaces after exposure to different oxidation conditions (either exposed to air or oxidized in pH 9 solution), in addition to high-resolution photoemission spectra from individual pixel areas of the images. Investigation of the homogeneous chalcopyrite sample allowed for the identification of step edges using the topography SPEM image, and high-resolution S 2*p* spectra acquired from the different parts of the sample image revealed a similar rate of surface oxidation from solution exposure for both step edge and a nearby terrace site. SPEM was able to successfully distinguish between chalcopyrite and bornite on the heterogeneous sample containing both minerals, based upon sulfur imaging. The high-resolution S 2*p* spectra acquired from the two regions highlighted the faster air oxidation of the bornite relative to the chalcopyrite. Differentiation between chalcopyrite and pyrite based upon contrast in SPEM images was not successful, owing to either the poor photoionization cross section of the Cu and Fe 3*p* electrons or issues with rough fracture of the composite surface. In spite of this, high-resolution S 2*p* spectra from each mineral phase were successfully obtained using a step-scan approach.

## 1. Introduction

Froth flotation is the major industrial process used to separate valuable metal sulfide minerals from worthless ore components. Successful separation by flotation relies on differences between the surface hydrophobicity of the minerals in the ore. Bubbles rise through a suspension of ground ore, and the mineral particles with sufficient hydrophobic character are able to be captured by the bubbles and carried to the surface where they are recovered, while hydrophilic mineral particles remain in the suspension (Wills & Napier-Munn, 2005). Effective flotation relies on careful control of mineral surface chemistry, particularly oxidation. The oxidation of metal sulfides proceeds *via* the diffusion of metal ions to the surface

from near-surface layers; the diffused metal ions oxidize to form a metal hydroxide and their absence from the mineral lattice leaves the near-surface layers metal depleted and sulfur rich (Buckley & Woods, 1984; Yin *et al.*, 1995, 2000; Fairthorne *et al.*, 1997; Vaughan *et al.*, 1997; Harmer *et al.*, 2006). Mild oxidation produces a surface rich in hydrophobic polysulfide species, but extensive oxidation results in high concentrations of hydrophilic metal hydroxides (Hayes *et al.*, 1987; Zachwieja *et al.*, 1989; Senior & Trahar, 1991; Fairthorne *et al.*, 1997). Conventional X-ray photoelectron spectroscopy (XPS) has been instrumental in the study of oxidation products formed on sulfide minerals (Brion, 1980; Buckley & Woods, 1984; Buckley, 1994), and use of synchrotron radiation has significantly improved the understanding of mineral surface chem-

istry, particularly the initial surface states of surfaces produced by fracture (Harmer *et al.*, 2004, 2005, 2009; Pratt, 2004; Buckley *et al.*, 2007).

The key advantage of XPS and synchrotron XPS (SXPS) in mineral studies is the detailed information that can be determined from high-resolution spectra. However, both conventional and synchrotron XPS are unable to provide high-spatial-resolution (micrometre/submicrometre) images of mineral surfaces that would enable one to identify and follow the development of oxidation products on heterogeneous samples, *i.e.* those that contain more than one mineral phase, and/or contain significant regions of impurities. This level of complexity is commonplace in real mineral systems, resulting in oxidation products not forming uniformly across mineral surfaces (Smart *et al.*, 2003), and oxidation rates varying owing to defect sites, crystal faces, step edges and the nature of the impurities (Buckley *et al.*, 1988; Smart *et al.*, 1998, 2003; Al-Harashseh *et al.*, 2006; Harmer *et al.*, 2006). When heterogeneous mineral samples have sufficiently large well defined macroscopic regions of different mineral phases (*e.g.* millimetre-sized regions), SXPS can be used to follow the development of surface chemistry on the different regions (Acres *et al.*, 2010a,c). However, such analysis does not allow one to interrogate specific surface features on the micrometre/submicrometre length scale. ToF-SIMS (time-of-flight secondary ion mass spectrometry) is one technique used to produce surface chemical maps of metal sulfide minerals with micrometre-level spatial resolution (Smart *et al.*, 2000, 2003; Khmeleva *et al.*, 2005; Harmer *et al.*, 2006; Priest *et al.*, 2008). However, ToF-SIMS provides limited chemical information and does not have sufficient spatial resolution to isolate small (submicrometre) initial patchy oxidation products that have been observed in atomic force microscopy (AFM) and scanning tunnelling microscopy studies (Kim *et al.*, 1994; Farquhar *et al.*, 2003).

The distribution of oxidation products is not the only heterogeneity of interest on mineral surfaces. Many natural sulfide minerals contain inclusions of other minerals, have variations in texture, and can contain other impurities, such as other metal ions [*e.g.* sphalerite, ZnS, which can contain high levels of Fe atoms (Harmer *et al.*, 2008)]. As with oxidation features, these inclusions and textural effects can occur on the submicrometre length scale. It is important to be able to not only identify the presence of species on surfaces using high-resolution photoemission spectroscopy but also the distribution of said species across the surface. The ideal experiment to study the distribution of small oxidation products, adsorbed metal ions and small disseminated mineral inclusions (and their individual oxidation) would combine the high spatial resolution of AFM with the high spectral resolution of XPS. Scanning photoemission microscopy (SPEM) is one such advanced synchrotron technique which combines surface-selective chemical imaging (as opposed to elemental imaging techniques that see deep into the bulk of a sample, *e.g.* energy-dispersive X-ray analysis with an analysis depth of multiple micrometres) with high spatial resolution (Ko *et al.*, 1998; Chuang *et al.*, 2001; Hong *et al.*, 2001; Klauser *et al.*, 2005; Kang

*et al.*, 2006). SPEM operates on the same principle as XPS, using a 100 nm focused synchrotron X-ray beam to excite photoelectrons from the surface. Scanning the sample stage in *x* and *y* using stepper motors or piezoelectric crystals (as with AFM) produces a surface-sensitive/specific chemical map of the surface, with submicrometre spatial resolution. From such images it is then possible to take high-resolution XPS spectra from selected points on the image, an ability that allows specific features to be analysed.

We have used SPEM to study homogeneous samples of the important copper mineral chalcopyrite ( $\text{CuFeS}_2$ ) that had been fractured and air oxidized as well as fractured and oxidized in a pH 9 solution of KOH for 30 min. In addition we have used SPEM to investigate the fractured air-oxidized surfaces of two heterogeneous samples of chalcopyrite with two common inclusions: one with bornite ( $\text{Cu}_5\text{FeS}_4$ ) to determine whether SPEM is capable of distinguishing between regions with the same elemental components, but different stoichiometry; and another with pyrite ( $\text{FeS}_2$ ) to determine whether SPEM imaging for an element unique to one phase can be employed for phase differentiation. In all cases high-resolution S 2*p* XPS spectra were obtained from specific regions observed in the SPEM images.

## 2. Experimental

### 2.1. Minerals and materials

The homogeneous chalcopyrite used in this study originated from the Huanzala Mine, Huallanca District, Huanuco Department, Peru, and was provided by the South Australian Museum, Adelaide (no catalogue number). Two heterogeneous samples of chalcopyrite were also provided by the South Australian Museum: a sample of chalcopyrite with bornite originating from Olympic Dam operations, Roxby Downs, South Australia (museum catalogue number G19341), and a sample of chalcopyrite with pyrite from the Geko Mine, Northern Territory, Australia (museum catalogue number G14939).

The purity and stoichiometry of the sample were confirmed using a CAMECA SX51 electron microprobe operating at 20 kV and 20 nA. Measurements were taken from ten points on each region and averaged: homogeneous Peruvian chalcopyrite  $\text{Cu}_{1.02}\text{Fe}_{1.01}\text{S}_2$ , no impurities above 0.03%; heterogeneous chalcopyrite with bornite from Roxby Downs, chalcopyrite  $\text{Cu}_{0.99}\text{Fe}_{0.99}\text{S}_{2.02}$ , no impurities above 0.02%, bornite  $\text{Cu}_{4.92}\text{FeS}_{4.08}$ , no impurities above 0.01%; heterogeneous chalcopyrite with pyrite from Geko Mine, chalcopyrite  $\text{CuFeS}_{2.05}$ , no impurities above 0.02%, pyrite  $\text{FeS}_{2.03}$ , no impurities above 0.02%.

Ultrapure water was produced on a Millipore MilliQ Element system with a resistivity of  $18.0 \text{ M}\Omega \text{ cm}^{-1}$ . KOH was produced by dissolving reagent-grade (>90%) KOH in ultrapure water.

### 2.2. Surface preparation

Mineral samples were fractured in air and mounted on the SPEM sample holder using conductive carbon tape. Samples

experienced approximately 15 min of air oxidation before being introduced into vacuum. A sample of Peruvian chalcocopyrite was fractured and immediately immersed in a pH 9 KOH solution for 30 min, then rinsed in fresh pH 9 KOH to stop any solution species from drying down onto the surface. Finally, surfaces were dried using a lint-free laboratory tissue without touching the surface to be analysed.

### 2.3. SPEM analysis

Surface chemical imaging on a submicrometre length scale was performed using SPEM at the National Synchrotron Radiation Research Centre, Taiwan, on beamline BL09A. The insertion device was a U5 undulator with a spherical-grating monochromator, and an incident photon energy of  $h\nu = 380$  eV was used in order to maximize flux while retaining high-energy resolution and for ease of X-ray focusing. The pressure in the analysis chamber was  $6 \times 10^{-9}$  torr or better during analysis.

SPEM utilizes a beam of synchrotron X-rays focused to a 100 nm spot by a zone plate and optical selection aperture to excite photoelectrons from the sample into a hemispherical energy analyser. Images were produced by rastering the sample stage in  $x$  and  $y$  under the 100 nm beam. Fast rough images with micrometre resolution over a larger area were produced using stepper motors to control the rastering, while images of smaller areas with submicrometre resolution and pixel sizes of 500 nm were produced using piezoelectric crystals to raster the sample stage. In order to produce sharp images of the surface the sample was moved in the  $z$  direction until maximum focus was achieved in the images. To assist in focusing, a supported carbon grid on a gold TEM grid was attached to the sample to provide a regular pattern with sharp edges. When a sharp image was acquired from the grid, the stage was moved to image the desired part of the surface and the focus was fine-tuned to account for slight  $z$  differences between the grid and sample surface.

Photoelectrons emitted from the samples were energy analysed using a hemispherical analyser and detected using a 16-channel detector. Each channel on the detector received signal from a slightly different energy over a small energy range encompassing a photoemission peak of a particular element. The energy range required was determined through the acquisition of a photoemission survey scan of the sample. By acquiring a signal across all 16 elements from each sample, it was possible to build up a map of the surface concentration of the selected element by dividing a peak channel by a background channel to remove the influence of topography. This procedure was repeated for a number of elements of interest, as identified from the initial survey scan for each sample. Given the incident photon energy (380 eV), the depth of the surface probed in the image acquisition was the uppermost nine to twelve monolayers with approximately 40% of the signal originating from the first three to four monolayers. Sulfur images were produced using the S  $2p$  peak, iron using the Fe  $3p$  peak and copper using the Cu  $3p$  peak.

The chemical maps were used to identify regions of interest from which high-resolution photoemission spectra were acquired to obtain detailed chemical bonding information. These high-resolution spectra were acquired from a specific pixel area of the imaged surface after acquisition of the surface chemical image (pixel area was dependent on the initial imaging parameters). Survey spectra were also acquired from each investigated pixel area. Survey spectra peak heights were normalized by dividing the peak height by the background next to the peak, similar to topography removal for the images

### 2.4. Peak fitting

Sulfur  $2p$  peaks occur as doublets (S  $2p_{3/2}$  and S  $2p_{1/2}$ ) as a result of spin-orbit splitting. The  $2p_{3/2}$  is the stronger peak with the  $2p_{1/2}$  peak being half its intensity and shifted by 1.19 eV to higher binding energy. For clarity, only the S  $2p_{3/2}$  peaks have been displayed in the figures. Peaks fitted to the high-resolution S  $2p$  spectra use a summed Gaussian-Lorentzian function to describe the convoluted Gaussian/Lorentzian line shapes of the peaks. The weighting used was 80% Gaussian and 20% Lorentzian. Positions drawn from the literature were used to assign species to peaks and limit peak positions during fitting. Background fitting was performed using the Shirley method (Shirley, 1972). In addition to the S  $2p$  doublets, an energy-loss feature has been fitted for chalcocopyrite, pyrite and bornite which relates to charge transfers into S  $3p$ -Fe  $3p$  molecular orbitals (Fujisawa *et al.*, 1994; Harmer *et al.*, 2004, 2005). The peak attributed to polysulfides has a broader full width at half-maximum than the bulk monosulfide and surface polysulfide because this peak is representing several different length sulfur oligomers that are difficult to resolve individually with any degree of confidence (Buckley *et al.*, 1984; Zachwieja *et al.*, 1989; Mielczarski *et al.*, 1996; Smart *et al.*, 2000).

## 3. Results and discussion

### 3.1. Homogeneous chalcocopyrite

SPEM images of fractured air-oxidized homogeneous chalcocopyrite are shown in Fig. 1. The images are from a  $500 \times 500$   $\mu\text{m}$  region of the fractured mineral surface, recorded with a pixel size of 5  $\mu\text{m}$ . The image in Fig. 1(a) is produced using an energy channel corresponding to the background energy in a S  $2p$  scan. Since there are no peaks at the energy used to produce this image it provides an indication of sample topography since the only variation in signal intensity will arise from height differences relative to the focal point of the analyser lens. The topography image indicates that the fracture surface is imperfect, as expected for chalcocopyrite; like most other copper sulfide minerals, chalcocopyrite has poor cleavage and is therefore more likely to break to reveal a conchoidal fracture surface, without the dominance of a particular crystal plane. Some darker regions are also present, most likely due to the presence of voids/pits in the fracture surface. Fig. 1(b) shows a topography-corrected image of

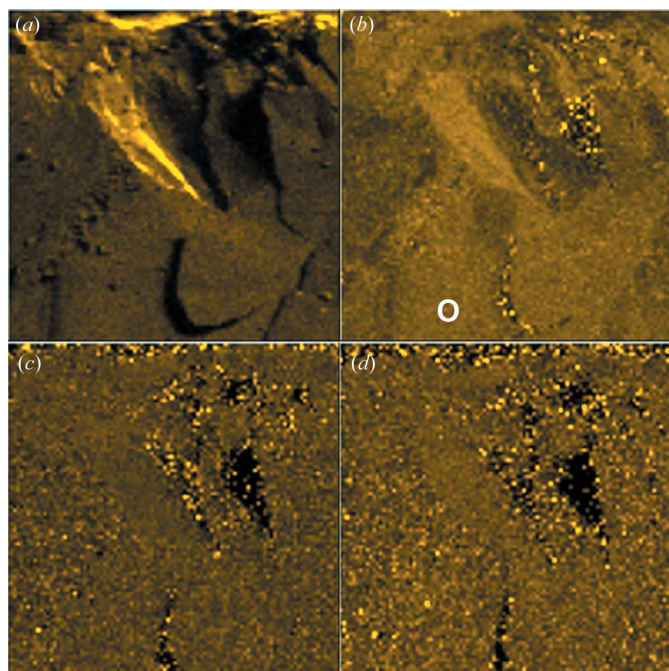


**Figure 1**  
500 × 500 μm SPEM images from fractured air-oxidized chalcopyrite. (a) Background channel showing topography, (b) topography-corrected S 2p, (c) topography-corrected Cu 3p and (d) topography-corrected Fe 3p.

sulfur abundance, constructed using the energy channel corresponding to the major S 2p peak in the multichannel spectrum. There appear to be some variations across the area imaged after the contrast is increased. Figs. 1(c) and 1(d) are topography-corrected images of copper and iron, respectively, recorded using the maximum intensity of the metal atom 3p photoemission peak. Neither image shows any clear variance. The more pixelated portions of the topography-corrected images correspond to voids on the sample surface, as seen in the topography image in Fig. 1(a).

Fig. 2 shows SPEM images obtained from a fractured homogeneous chalcopyrite sample that had been immersed in pH 9 KOH for 30 min prior to SPEM analysis. Fig. 2(a) is a large-scale (500 × 500 μm) S 2p background, similar to that obtained for the air-oxidized chalcopyrite sample shown in Fig. 1(a). The fracture surface of this sample is not as rough as the air-oxidized sample, although there is some evidence of small pits in the image. Figs. 2(b) and 2(c) are fine-detail (50 × 50 μm) images with a pixel size of 250 nm collected from the area indicated by the box in Fig. 2(a). This region was chosen for high-resolution imaging because it appears to exhibit a series of step edges. Fig. 2(b) is also a S 2p background image while Fig. 2(c) is the topography-corrected S 2p peak image showing no variation across this imaged region. Iron and copper images of the large area in Fig. 2(a) again showed no variation and are not shown here, nor are any variations observed for S 2p over the larger area.

High-resolution S 2p spectra taken from single-pixel areas chosen from the images in Figs. 1 and 2 (general locations identified using the white circles on the images, although the

**Table 1**  
S 2p quantification for homogeneous chalcopyrite.

Sample	Species	2p <sub>3/2</sub> position (eV)	FWHM (eV)	Area contribution (%)
Air-oxidized	Bulk monosulfide <sup>a</sup>	161.1	0.7	54
	Disulfide <sup>b,c</sup>	161.7	0.7	18
	Polysulfide <sup>b,c</sup>	162.9	1.4	19
	Energy loss <sup>a,d</sup>	163.9	2.6	9
pH 9 ox Spot 1	Bulk monosulfide <sup>a</sup>	161.1	0.8	47
	Disulfide <sup>b,c</sup>	161.7	0.8	18
	Polysulfide <sup>b,c</sup>	163.0	1.6	27
pH 9 ox Spot 2	Bulk monosulfide <sup>a</sup>	161.1	0.7	45
	Disulfide <sup>b,c</sup>	161.7	0.7	17
	Polysulfide <sup>b,c</sup>	163.0	1.6	31
	Energy loss <sup>a,d</sup>	163.9	2.3	7

Reference: <sup>a</sup>Harmer *et al.* (2004). <sup>b</sup>Buckley & Woods (1984). <sup>c</sup>Harmer *et al.* (2006). <sup>d</sup>Fujisawa *et al.* (1994).

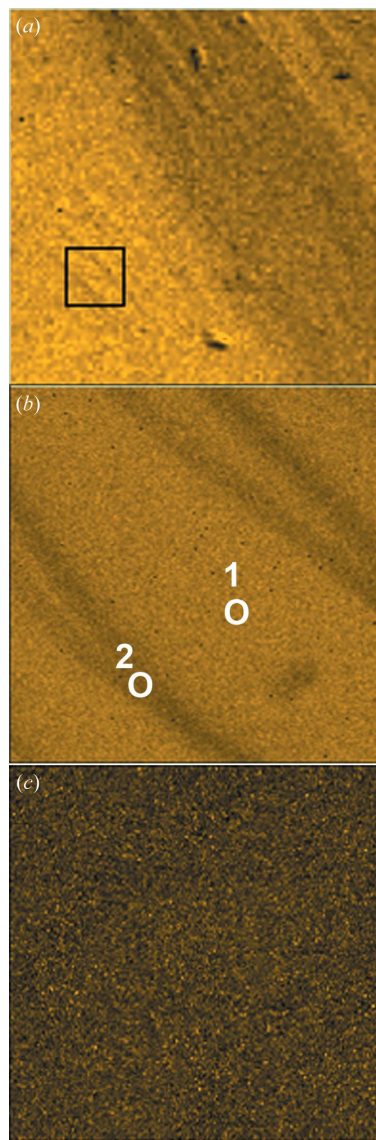


**Figure 2**  
SPEM images from pH 9 oxidized chalcopyrite. (a) 500 × 500 μm background image showing topography; (b) 50 × 50 μm background image from the region indicated by the square in (a); (c) 50 × 50 μm topography-corrected S 2p image from the same region as (b).

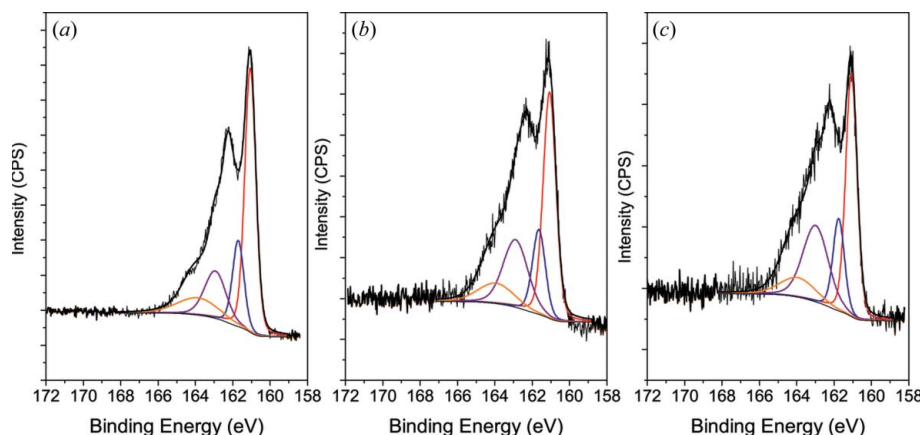


**Figure 3**

S 2*p* SXPS spectra collected at  $h\nu = 380$  eV from (a) air-oxidized homogeneous chalcopyrite [point indicated in Fig. 1(b)], (b) pH 9 oxidized homogeneous chalcopyrite from point 1 in Fig. 2(b), and (c) pH 9 oxidized homogeneous chalcopyrite from point 2 in Fig. 2(b). Plots also include deconvoluted peak components from the sulfur species contributing to the S 2*p* profile (only 2*p*<sub>3/2</sub> spin orbit components displayed): red, monosulfide; blue, disulfide; purple, polysulfide; orange, energy-loss feature.

actual pixel size is much smaller than the regions circled) are presented in Fig. 3. Fig. 3(a) was collected from the air-oxidized sample while Figs. 3(b) and 3(c) are from points 1 (terrace) and 2 (step), respectively, on the pH 9 oxidized sample. The quantifications for these spectra are presented in Table 1. Sulfur 2*p* spectra of oxidized chalcopyrite are well reported in the literature and consist of four major components: three doublets representing bulk monosulfide, disulfide and polysulfide, in addition to the energy-loss feature. The majority of the sulfur signal from the air-oxidized sample corresponds to bulk monosulfide at 161.1 eV (Harmer *et al.*, 2004) with 54% of the total S 2*p* area. Disulfides and polysulfides at 161.7 eV (Buckley *et al.*, 1984; Harmer *et al.*, 2006) and 162.9 eV (Buckley *et al.*, 1984; Harmer *et al.*, 2006), respectively, contribute approximately the same amount to the S 2*p* area with disulfides at 18% and polysulfides at 19%. No evidence of sulfate at an energy of around 168 eV (Buckley *et al.*, 1984) is observed.

Both positions on the pH 9 oxidized chalcopyrite sample show a lower proportion of bulk monosulfide and higher surface polysulfide contribution compared with the air-oxidized chalcopyrite, indicating a greater degree of oxidation has occurred owing to solution exposure. Spot 1 has a bulk monosulfide contribution at 161.1 eV of 47% while the bulk contribution from spot 2 is 45%. Both spots 1 and 2 have a higher concentration of surface polysulfides at 163 eV, with 27% from spot 1 and 31% at spot 2 (compared with 19%

for the air-oxidized sample); the total sulfur at the different surface points on the solution-oxidized sample was uniform. All three spectra have approximately the same amount of disulfide species: 18% on spot 1 and 17% on spot 2 compared with the 18% contribution from the air-oxidized sample. The S 2*p* spectra from spot 1 and spot 2 are quite similar, indicating that there is little difference in the degree of oxidation between step edges and faces/terraces. It is possible that the polycrystalline nature of the chalcopyrite has resulted in an averaging of the oxidation rate for the two different surface areas, and that step/terrace differences might be more apparent for a mineral sample with a greater single-crystal orientation, such as sphalerite (ZnS).

### 3.2. Heterogeneous chalcopyrite with bornite

Fig. 4 presents  $500 \times 500 \mu\text{m}$  SPEM images from air-oxidized heterogeneous chalcopyrite with bornite. The topography image obtained using the background energy channel of the S 2*p* energy region is given in Fig. 4(a), and Cu 3*p* and Fe 3*p* images (topography-corrected) are given in Figs. 4(b) and 4(c), respectively. These two images have had their contrast slightly increased for clarity. The differences between the regions on the iron and copper images are quite subtle and

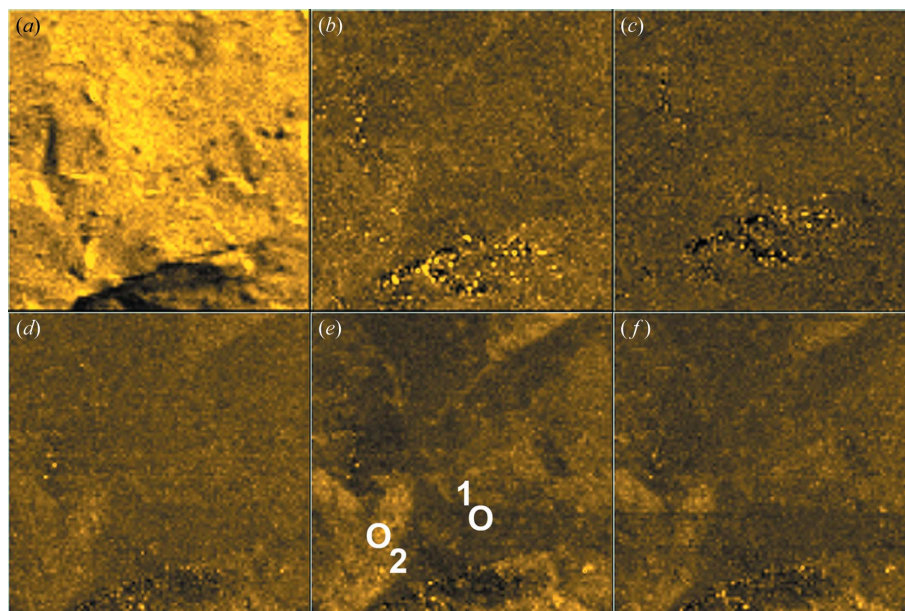


**Figure 4**

$500 \times 500 \mu\text{m}$  SPEM images from fractured air-oxidized chalcopyrite with bornite. (a) Background channel indicating topography and topography-corrected images from (b) Cu 3*p* and (c) Fe 3*p*. Topography-corrected images (d), (e) and (f) are from the S 2*p* signal from an energy channel on the multi-element detector of approximately 164 eV (d), 162 eV (e) and 161 eV (f).

**Table 2**

S 2p quantification for air-oxidized chalcopyrite with bornite.

Sample	Species	2p <sub>3/2</sub> position (eV)	FWHM (eV)	Area contribution (%)
Point 1 Chalcopyrite	Bulk monosulfide <sup>a</sup>	161.1	0.7	53
	Disulfide <sup>b,c</sup>	161.8	0.7	19
	Polysulfide <sup>b,c</sup>	162.7	1.5	18
	Energy loss <sup>a,d</sup>	163.9	2.5	8
	Sulfate <sup>b</sup>	168.1	1.3	2
Point 2 Bornite	Fully coordinated bulk <sup>e</sup>	161.0	0.8	45
	Disulfide <sup>b,c</sup>	161.7	0.8	20
	Polysulfide <sup>b,c</sup>	163.0	1.7	27
	Energy loss <sup>a,d</sup>	163.9	2.3	8

Surface stoichiometry (from survey spectrum): chalcopyrite Cu 1.5 Fe 1.5 S 1.93; bornite Cu 1.7 Fe 1.34 S 4.2.

Reference: <sup>a</sup>Harmer *et al.* (2004), <sup>b</sup>Buckley & Woods (1984), <sup>c</sup>Harmer *et al.* (2006), <sup>d</sup>Fujisawa *et al.* (1994), <sup>e</sup>Harmer *et al.* (2005).

difficult to discern owing to the poor signal from the copper and iron 3p photoemission peaks. Nevertheless, in the copper image it is still possible to discern regions of high and low Cu concentration, with the high copper regions most likely being bornite (Cu<sub>5</sub>FeS<sub>4</sub>) as opposed to chalcopyrite (CuFeS<sub>2</sub>). However, the Fe 3p image (Fig. 4c) appears uniform. The three remaining images in Fig. 4 [*i.e.* Figs. 4(d)–4(f)] are S 2p images, with each image being constructed from the signal from different energy channels on the multi-element detector. None of the three S 2p images were contrast altered. The approximate energy values for the images are 164 eV (d), 162 eV (e) and 161 eV (f). These energies represent the high-energy, middle and lower-energy sections of the S 2p photoemission peak, and all three images have regions of higher and lower sulfur signal. It is quite clear that, as one passes from the high-energy side (low S 2p signal) to the low-energy side of the photoemission peak (higher S 2p signal), the contrast between the high and low sulfur regions is enhanced, and that the high sulfur regions correlate with the high copper regions from Fig. 4(b).

To verify whether the initial identification of the two mineral phases was correct, two single-pixel areas were selected for high-resolution S 2p spot spectra (positions indicated in Fig. 4e) and the resulting spectra presented in Fig. 5 and the spectral quantification in Table 2. The S 2p spectrum from spot 1 (Fig. 5a) closely resembles the spectrum from air-oxidized homogeneous chalcopyrite (Fig. 3a) with a contribution of 53% from bulk monosulfide at 161.1 eV and di- and polysulfide contributions of 19% and 18%, respectively. In addition to the peaks observed on the homogeneous air-oxidized sample there is also a small sulfate peak at 168.1 eV contributing 2% to the total S 2p spectrum. The S 2p spectrum from spot 2 (Fig. 5b) indicates a greater degree of oxidation than that of spot 1. Di- and polysulfide contributions from this spot are higher, only slightly at 20% for disulfide at 161.7 eV but significantly at 27% for polysulfide. This increased oxidation would be expected from bornite [45% at 161.0 eV (Harmer *et al.*, 2005)] which has a much faster oxidation rate than chalcopyrite in air (Buckley & Woods, 1984). Contributions from fully coordinated bulk sulfur in bornite are lower

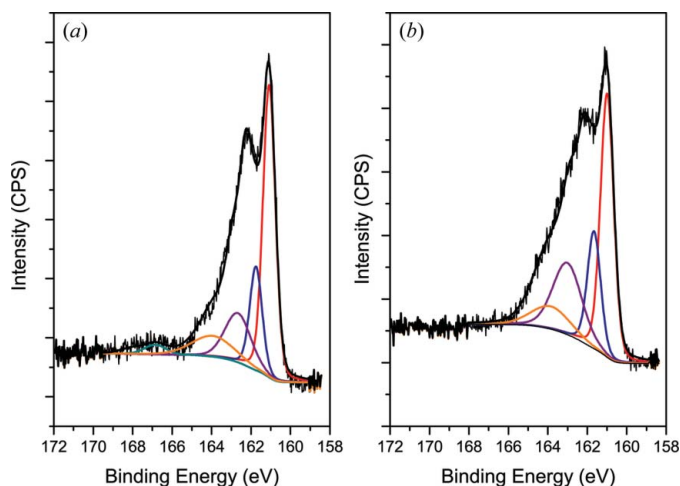


**Figure 5**

S 2p SXPS spectra collected at  $h\nu = 380$  eV from air-oxidized heterogeneous chalcopyrite with bornite. (a) Chalcopyrite phase (point 1 in Fig. 4e) and (b) bornite phase (point 2 in Fig. 4e). Plots also include deconvoluted peak components from the sulfur species contributing to the S 2p profile (only 2p<sub>3/2</sub> spin orbit components displayed): red, bulk sulfide; blue, disulfide; purple, polysulfide; orange, energy-loss feature; green, sulfate.

than the chalcopyrite phase at point 1 because the oxidation layer is thicker at point 2 (suggested by the increased disulfides and polysulfides) with the result that less of the bulk mineral is probed. The conclusion regarding the identification of the two phases based on the S 2p spectra is supported by the survey scans for both points (not shown) that indicate a higher Cu:Fe ratio on point 2 compared with point 1.

These results indicate that distinguishing between chalcopyrite and bornite on a slightly oxidized sample is possible using SPEM at this surface-sensitive photon energy. It is possible that with further oxidation it would become more difficult to distinguish between the two regions, as bornite will become more like chalcopyrite as iron migrates to its surface and near-surface layers. At this length scale, no growth of oxidation products is visible as has been observed at smaller length scales in other studies (Farquhar *et al.*, 2003; Harmer *et al.*, 2006) but in this case the degree of oxidation is only small and from brief air exposure rather than induced electrochemically or through surface treatment.

### 3.3. Heterogeneous chalcopyrite with pyrite

SPEM imaging of an air-oxidized sample containing both chalcopyrite and pyrite is shown in Fig. 6. It is clear from these images that there is no contrast between phases in either the Cu 3p (Fig. 6b) or Fe 3p (Fig. 6c) images. For comparison a backscattered electron (BSE) scanning electron micrograph of a similar region on another sample cut from the same bulk mineral is presented as Fig. 7, with the lighter regions being chalcopyrite and the darker regions pyrite.

Several different areas were imaged and at no time was differentiation between mineral phases based on copper or iron images possible. A systematic search was conducted in an attempt to manually identify two phases based on survey

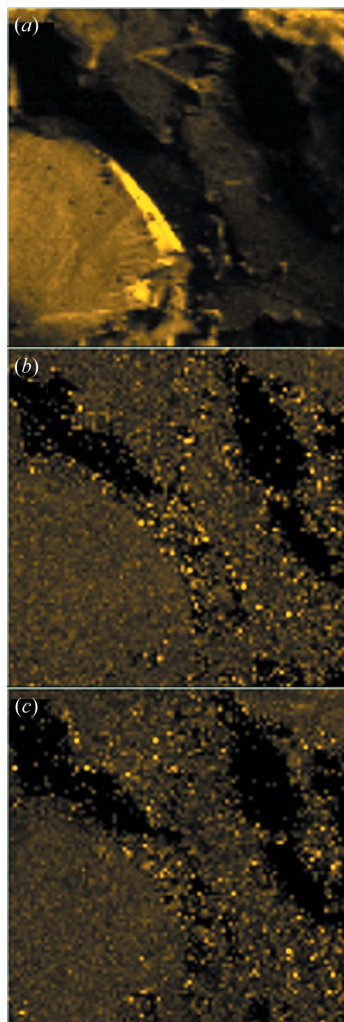


**Figure 6**  
500 × 500 μm SPEM images from fractured air-oxidized chalcopyrite with pyrite. (a) Background channel showing topography, (b) topography-corrected Cu 3p, (c) topography-corrected Fe 3p.

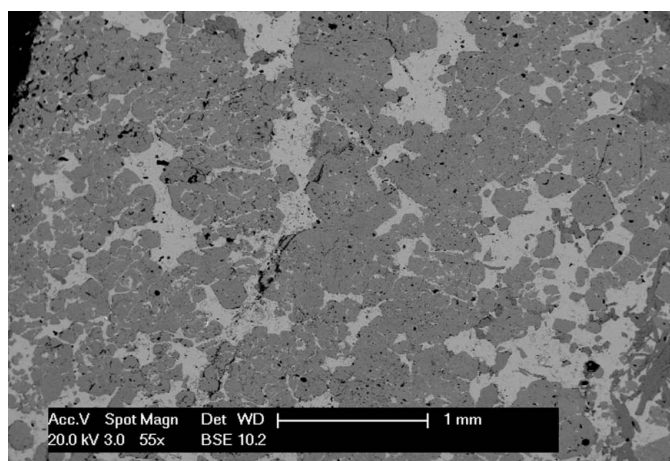


**Figure 7**  
Backscattered scanning electron micrograph of a polished cross section from a polished mixed chalcopyrite/pyrite region similar to that investigated by SPEM. The lighter region is chalcopyrite and the darker grey is pyrite. Collected at 20 kV accelerating voltage.

spectra by scanning the stepper motors in one direction in discrete increments in the area imaged in Fig. 6. Two points were located whose survey spectra indicated that one should be chalcopyrite and the other pyrite (based on the absence of a Cu 3p peak in the survey scan of one region) and high-resolution S 2p spectra were collected from single-pixel areas at these points, presented here in Fig. 8.

The S 2p profile in the spectrum in Fig. 8(a) indicates that this point is on chalcopyrite, and the identification is confirmed by the survey scan from this point, as shown in Fig. 8(c), with both Cu 3p and Fe 3p peaks visible in the spectrum. A quantification of the peak contributions in the S 2p spectrum from this sample is given in Table 3. The deconvolution indicates that the chalcopyrite region in the chalcopyrite/pyrite sample is more oxidized than the air-oxidized homogeneous chalcopyrite (Fig. 3a) or the air-oxidized chalcopyrite with bornite (Fig. 5a), with a bulk monosulfide contribution at 161.1 eV of 49% and a polysulfide contribution at 163.1 eV of 26% while the disulfides at 161.7 eV are approximately the same as the other two air-oxidized chalcopyrite regions at 17%. The reason for the difference in the amount of polysulfide on the chalcopyrite region of this sample relative to the other two chalcopyrite samples is not immediately apparent. The difference is larger than the expected uncertainty in the fitting percentages (likely to be ±1–2% based on repeated measurements of XPS spectra from similar samples). The only major difference

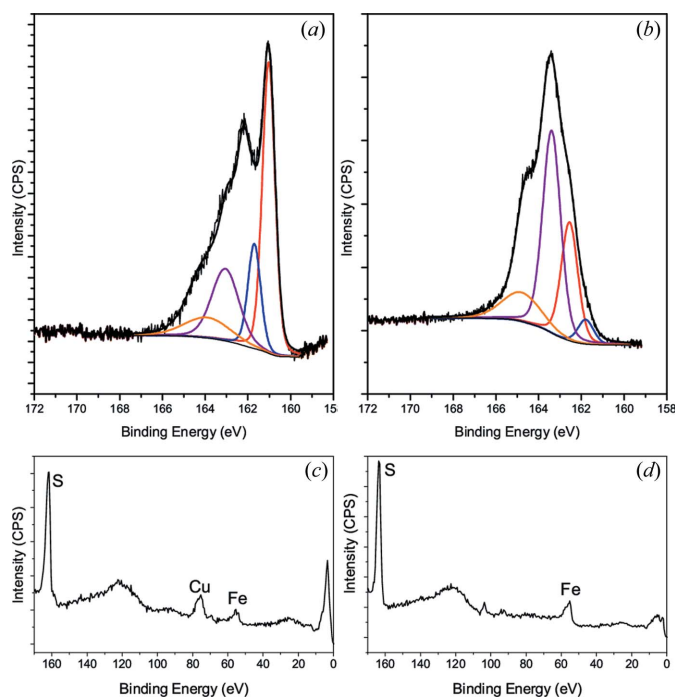


**Figure 8**  
S 2p SXPS spectra collected at  $h\nu = 380$  eV from air-oxidized heterogeneous chalcopyrite with pyrite. (a) Chalcopyrite region (red, monosulfide; blue, disulfide; purple, polysulfide; orange, energy-loss feature) and (b) pyrite region (red, bulk disulfide; blue, surface disulfide; purple, polysulfide; orange, energy-loss feature). Survey SXPS spectra from the two regions are shown underneath the S 2p SXPS spectra: (c) chalcopyrite region and (d) pyrite region.

**Table 3**

S 2*p* quantification for air-oxidized chalcopyrite with pyrite.

Sample	Species	2 <i>p</i> <sub>3/2</sub> position (eV)	FWHM (eV)	Area contribution (%)
Chalcopyrite	Bulk monosulfide <sup>a</sup>	161.1	0.7	49
	Disulfide <sup>b,c</sup>	161.7	0.7	17
	Polysulfide <sup>b,c</sup>	163.1	1.5	26
	Energy loss <sup>a,d</sup>	163.9	2.5	8
Pyrite	Bulk disulfide <sup>e</sup>	162.6	0.9	29
	Disulfide <sup>b,c</sup>	161.8	0.8	6
	Polysulfide <sup>b,c</sup>	163.4	1.7	54
	Energy loss <sup>a,d</sup>	164.6	2.3	11

Surface stoichiometry (from survey spectrum): chalcopyrite Cu 1.74 Fe 1.76 S 4.40; pyrite Fe 1.75 S 5.51.

Reference: <sup>a</sup>Harmer *et al.* (2004), <sup>b</sup>Buckley & Woods (1984), <sup>c</sup>Harmer *et al.* (2006), <sup>d</sup>Fujisawa *et al.* (1994), <sup>e</sup>Buckley & Woods (1987).

between the chalcopyrite samples used in this work is the grain size/fracture characteristics. Such differences are influential in the subsequent air and/or solution oxidation of the surfaces (*e.g.* Acres *et al.*, 2010*a*). It is likely that small differences in morphology of the surface, owing to the varying grain size/fracture characteristics, is behind the slightly different development of surface oxidation products from the exposure to air before analysis, owing to a variation in surface area and/or differences in surface reactivity.

The second point analysed for the acquisition of a high-resolution S 2*p* scan was deemed to be pyrite based initially on the survey scan from this point, as shown in Fig. 8(*d*), with the Fe 3*p* peak visible in the spectrum, unaccompanied by the Cu 3*p* peak. This identification was confirmed by the acquisition of the S 2*p* spectrum (Fig. 8*b*), with the profile indicating clearly the presence of pyrite (Harmer & Nesbitt, 2004). The S 2*p* spectrum of pyrite is distinctly different from that of chalcopyrite. The origin of this difference lies in the crystal structure of the two minerals. Sulfur in bulk pyrite is disulfide (Harmer & Nesbitt, 2004), producing a very strong doublet with the major component at 162.6 eV (29%). Bulk sulfur in chalcopyrite is monosulfide (Harmer *et al.*, 2004), resulting in a very different S 2*p* profile, with a dominant doublet at a lower binding energy of 161.3 eV. In addition to the bulk disulfide peak, oxidized pyrite also has a surface disulfide peak, which in the spectrum in Fig. 8(*b*) is seen as a doublet with major component at 161.8 eV (contributing 6% to the overall profile area). The largest doublet in the fitted spectrum is that of surface polysulfide, with a major doublet component at 163.4 eV (Harmer & Nesbitt, 2004), contributing 54% to the overall profile area.

The inability to distinguish the two phases based upon the Cu 3*p* and Fe 3*p* SPEM images may be due to two possible reasons. First, the intensity of these peaks may be too low to produce sufficient contrast in the SPEM images. The 3*p* peaks for these two metals have a very low photoionization cross section at 380 eV and it is possible that the difference between the intensity of the Cu 3*p* peak from chalcopyrite and the background intensity at this part of the spectrum from pyrite may not have been sufficient to be detected. It is possible that access to the Cu 2*p* (~930 eV) and Fe 2*p* (~710 eV) peaks

may have resulted in differentiation between these two phases, but these peaks are not available at a photon energy of 380 eV. The potential for distinguishing between these two mineral phases with access to the 2*p* region is supported by the ability to distinguish between pyrrhotite (Fe<sub>7</sub>S<sub>8</sub>) and chalcopyrite using synchrotron photoemission electron microscopy (PEEM) (Acres *et al.*, 2010*b*), using the signal from *L*-edge X-ray absorption of Cu and Fe. The second possible explanation for the inability to distinguish between the chalcopyrite and pyrite phases is the rough topography of the sample. Such surface roughness, which was caused by the heterogeneous nature of the sample and the naturally poor cleavage of the two minerals, may have contributed to the low contrast in the Cu and Fe images obtained for this sample. Attempts were made to alter the topography correction method, using a different channel from the multi-element detector to determine whether the lack of contrast could be remedied in this way. No improvement was seen in the images. Future experiments using samples more amenable to smooth fracture, and a higher incident photon energy (to access the Fe and Cu 2*p* photoemission peak), are planned to investigate whether topography or peak intensity were the limiting factors in this study.

Differential charging on the sample owing to oxidation can be ruled out as a factor in the low contrast, as there was no change in the photoemission spectral peaks (position or width) over time, and the level of oxidation is mild (*i.e.* most likely limited to a few monolayers at the surface) owing to the short exposure to air before analysis.

#### 4. Conclusions

The capability to produce both high-spatial-resolution surface chemical images and high-energy-resolution SXPS spectra from selected points on such images makes SPEM an attractive technique for the study of sulfide mineral surface chemistry. SPEM imaging of homogeneous chalcopyrite was able to identify surface steps and terraces and then target individual regions for high-resolution S 2*p* spectra; such analysis is of use in studying how different crystal faces respond to reactions such as copper activation or surfactant adsorption. SPEM was able to successfully distinguish between chalcopyrite and bornite phases using S 2*p* imaging and to a lesser extent Cu 3*p* imaging, then used to selectively probe these two regions to produce high-resolution SR-XPS spectra. SPEM imaging was however, unable to differentiate between chalcopyrite and pyrite using Cu 3*p* imaging even though copper is not present in pyrite, a situation which would more than likely be rectified if a photon energy suitable to probe the Fe and Cu 2*p* photoemission peaks was able to be employed on this occasion. This study indicates that there is significant potential for the use of SPEM in studying small heterogeneities or surface reaction species on sulfide minerals, providing that care is taken in selecting workable mineral samples.

The authors would like to acknowledge financial support from the Australian Research Council Linkage Scheme

(AMSRI-LP0667828), AMIRA International, and the sponsors of AMIRA International Project P924: BHP/Billiton, Rio Tinto, Orica Explosives, Anglo Platinum, Xstrata Technology, Freeport McMoran and AREVA NC. The authors would like to thank Professor Allan Pring (South Australian Museum, Adelaide) for supplying the mineral samples. We acknowledge travel funding provided by the International Synchrotron Access Program (ISAP) managed by the Australian Synchrotron. The ISAP is an initiative of the Australian Government being conducted as part of the National Collaborative Research Infrastructure Strategy.

## References

- Acres, R. G., Harmer, S. L. & Beattie, D. A. (2010a). *Int. J. Miner. Process.* **94**, 43–51.
- Acres, R. G., Harmer, S. L. & Beattie, D. A. (2010b). *J. Synchrotron Rad.* **17**, 606–615.
- Acres, R. G., Harmer, S. L. & Beattie, D. A. (2010c). *Miner. Eng.* **23**, 928–936.
- Al-Harashsheh, M., Kingman, S., Rutten, F. & Briggs, D. (2006). *Int. J. Miner. Process.* **80**, 205–214.
- Brion, D. (1980). *Appl. Surf. Sci.* **5**, 133–152.
- Buckley, A. N. (1994). *Colloids Surf. A*, **93**, 159–172.
- Buckley, A. N., Hamilton, I. C. & Woods, R. (1984). *J. Appl. Electrochem.* **14**, 63–74.
- Buckley, A. N., Hamilton, I. C. & Woods, R. (1988). *Proceedings of the International Symposium on Electrochemistry in Mineral and Metal Processing II*, edited by P. E. Richardson and R. Woods, pp. 234–246. Pennington: The Electrochemical Society.
- Buckley, A. N., Skinner, W. M., Harmer, S. L., Pring, A., Lamb, R. N., Fan, L.-J., Yang, Y.-W. (2007). *Can. J. Chem.* **85**, 767–781.
- Buckley, A. N. & Woods, R. (1984). *Aust. J. Chem.* **37**, 2403–2413.
- Buckley, A. N. & Woods, R. (1987). *Appl. Surf. Sci.* **27**, 437–452.
- Chuang, T. J., Chan, Y. L., Chuang, P., Klauser, R., Ko, C. H. & Wei, D. H. (2001). *Appl. Surf. Sci.* **169–170**, 1–10.
- Fairthorne, G., Fornasiero, D. & Ralston, J. (1997). *Int. J. Miner. Process.* **49**, 31–48.
- Farquhar, M. L., Wincott, P. L., Wogelius, R. A. & Vaughan, D. J. (2003). *Appl. Surf. Sci.* **218**, 34–43.
- Fujisawa, M., Suga, S., Mizokawa, T., Fujimori, A. & Sato, K. (1994). *Phys. Rev. B*, **49**, 7155.
- Harmer, S. L., Mierczynska-Vasilev, A., Beattie, D. A. & Shapter, J. G. (2008). *Miner. Eng.* **21**, 1005–1012.
- Harmer, S. L. & Nesbitt, H. W. (2004). *Surf. Sci.* **564**, 38–52.
- Harmer, S. L., Pratt, A. R., Nesbitt, W. H. & Fleet, M. E. (2004). *Am. Miner.* **89**, 1026–1032.
- Harmer, S. L., Pratt, A. R., Nesbitt, H. W. & Fleet, M. E. (2005). *Can. Miner.* **43**, 1619–1630.
- Harmer, S. L., Skinner, W. M., Buckley, A. N. & Fan, L.-J. (2009). *Surf. Sci.* **603**, 537–545.
- Harmer, S. L., Thomas, J. E., Fornasiero, D. & Gerson, A. R. (2006). *Geochim. Cosmochim. Acta*, **70**, 4392–4402.
- Hayes, R. A., Price, D. M., Ralston, J. & Smith, R. W. (1987). *Miner. Process. Extr. Metall. Rev.* **2**, 203–234.
- Hong, I. H., Lee, T. H., Yin, G. C., Wei, D. H., Juang, J. M., Dann, T. E., Klauser, R., Chuang, T. J., Chen, C. T. & Tsang, K. L. (2001). *Nucl. Instrum. Methods Phys. Res. A*, **467–468**, 905–908.
- Kang, J. S., Kim, G., Lee, S. S., Choi, S., Cho, S., Han, S. W., Shin, H. J. & Min, B. I. (2006). *J. Magn. Magn. Mater.* **304**, e143–e145.
- Khmeleva, T. N., Georgiev, T. V., Jasieniak, M., Skinner, W. M. & Beattie, D. A. (2005). *Surf. Interface Anal.* **37**, 699–709.
- Kim, B. S., Hayes, R. A., Prestidge, C. A., Ralston, J. & Smart, R. S. C. (1994). *Appl. Surf. Sci.*, **78**, 385–397.
- Klauser, R., Chen, C. H., Huang, M. L., Wang, S. C., Chuang, T. J. & Zharnikov, M. (2005). *J. Electron Spectrosc. Relat. Phenom.* **144–147**, 393–396.
- Ko, C.-H., Klauser, R., Wei, D.-H., Chan, H.-H. & Chuang, T. J. (1998). *J. Synchrotron Rad.* **5**, 299–304.
- Mielczarski, J. A., Cases, J. M., Alnot, M. & Ehrhardt, J. J. (1996). *Langmuir*, **12**, 2519–2530.
- Pratt, A. (2004). *Surf. Interface Anal.* **36**, 654–657.
- Priest, C., Stevens, N., Sedev, R., Skinner, W. & Ralston, J. (2008). *J. Colloid Interface Sci.* **320**, 563–568.
- Senior, G. D. & Trahar, W. J. (1991). *Int. J. Miner. Process.* **33**, 321–341.
- Shirley, D. A. (1972). *Phys. Rev. B*, **5**, 4709.
- Smart, R. S. C., Amarantidis, J., Skinner, W. M., Vanier, L. L. & Grano, S. R. (2003). *Topics in Applied Physics*, Vol. 85, *Solid-Liquid Interfaces*, edited by K. Wandelt and S. Thurgate, pp. 3–60.
- Smart, R. S. C., Amarantidis, J., Skinner, W., Prestidge, C. A., La Vanier, L. & Grano, S. (1998). *Scanning Microsc.* **12**, 553–583.
- Smart, R. S. C., Jasieniak, M., Prince, K. E. & Skinner, W. M. (2000). *Miner. Eng.* **13**, 857–870.
- Vaughan, D. J., Becker, U. & Wright, K. (1997). *Int. J. Miner. Process.* **51**, 1–14.
- Wills, B. A. & Napier-Munn, T. (2005). *Wills' Mineral Processing Technology*, 7th ed., pp. 267–352. Oxford: Butterworth-Heinemann.
- Yin, Q., Kelsall, G. H., Vaughan, D. J. & England, K. E. R. (1995). *Geochim. Cosmochim. Acta*, **59**, 1091–1100.
- Yin, Q., Vaughan, D. J., England, K. E. R., Kelsall, G. H. & Brandon, N. P. (2000). *J. Electrochem. Soc.* **147**, 2945–2951.
- Zachwieja, J. B., McCarron, J. J., Walker, G. W. & Buckley, A. N. (1989). *J. Colloid Interface Sci.* **132**, 462–468.